

**Pulsed studies of intervalley transfer in  $\text{Al}_{0.35}\text{In}_{0.65}\text{As}$ : A paradigm for valley photovoltaics**R. Dixit,<sup>1</sup> B. Barut,<sup>2</sup> S. Yin,<sup>1</sup> J. Nathawat,<sup>1</sup> M. Randle,<sup>1</sup> N. Arabchigavkani,<sup>2</sup> K. He,<sup>1</sup> C.-P. Kwan,<sup>2</sup> T. D. Mishima,<sup>3</sup> M. B. Santos,<sup>3</sup> D. K. Ferry,<sup>4</sup> I. R. Sellers,<sup>3</sup> and J. P. Bird<sup>1</sup><sup>1</sup>*Department of Electrical Engineering, University at Buffalo, State University of New York, Buffalo, New York 14260-1900, USA*<sup>2</sup>*Department of Physics, University at Buffalo, State University of New York, Buffalo, New York 14260-1500, USA*<sup>3</sup>*Homer L. Dodge Department of Physics and Astronomy, The University of Oklahoma, 440 West Brooks Street, Norman, Oklahoma 73019, USA*<sup>4</sup>*School of Electrical, Computer, and Energy Engineering, Arizona State University, 85287-5706 Tempe, Arizona, USA*

(Received 29 April 2020; accepted 3 August 2020; published 27 August 2020)

$\text{Al}_{0.35}\text{In}_{0.65}\text{As}$  is a direct semiconductor whose multivalley conduction-band structure has been proposed for use in so-called *valley photovoltaics*. In such hot-carrier solar cells, energetic (hot) photocarriers are stored in satellite valleys away from the  $\Gamma$  point, allowing them to be extracted prior to thermalization and to thereby increase power-conversion efficiency. While prior theoretical work has highlighted the potential of  $\text{Al}_{0.35}\text{In}_{0.65}\text{As}$ —a widely used barrier material in electronic and optoelectronic devices, for use in valley photovoltaics—surprisingly little is known about its electrical properties, especially how these are impacted by the application of high fields. In this work, we therefore undertake a detailed characterization of the electrical properties of Te-doped (*n*-type)  $\text{Al}_{0.35}\text{In}_{0.65}\text{As}$ , over wide ranges of temperature (3–400 K) and electric field (<50 kV/cm). Using pulsed measurements to suppress the influence of Joule heating, we reveal the presence of clear negative-differential conductance in the current-voltage characteristics of the films, suggestive of the intervalley transfer of hot electrons. This conclusion is supported by the results of ensemble Monte Carlo simulations of the hot-carrier action, which confirm the connection of the observed negative-differential conductance to hot-electron transfer from the conduction-band ( $\Gamma$ ) minimum, to the side valleys at the *L* point. The quantitative features of the experimentally determined velocity-field curves are found to be in good agreement with the results of these calculations, providing further confidence in the role of the implied intervalley transfer mechanism. Overall, these results confirm the excellent potential of  $\text{Al}_{0.35}\text{In}_{0.65}\text{As}$  for use as the absorber material in hot-carrier solar cell technology.

DOI: [10.1103/PhysRevMaterials.4.085404](https://doi.org/10.1103/PhysRevMaterials.4.085404)**I. INTRODUCTION**

Recently, there has been renewed interest in high-efficiency single-band-gap solar cells using third-generation photovoltaics [1]. The most successful technology to have been demonstrated to date is the multijunction cell, which uses a cascade of different materials that are grown monolithically to optimally harness the solar spectrum [2]. More novel approaches under development include multiexciton-based devices, in which the absorption of high-energy single photons leads to the generation of two or more (multiple) electron-hole pairs [3], and intermediate-band solar cells [4], which harness lower-energy carriers typically lost via transmission. These devices are complex, however, and require technologically challenging architectures. As a result of the complexity, most of these latter approaches have not yielded any breakthroughs. Moreover, single-junction photovoltaic devices have yet to reach the single-band-gap Shockley-Queisser limit [5], so there remains a wide-open field for improved photovoltaic devices.

An alternative approach that has been proposed as a means to circumvent the Shockley-Queisser limit is the so-called hot-carrier solar cell [6]. In this technology, highly energetic

(hot) photogenerated carriers are extracted from the junction prior to thermalization, providing the potential to increase the power-conversion efficiency of a single-gap cell to greater than 50% [6,7]. Much of the recent work in the development of this technology has focused upon inhibiting the electron-phonon interaction (or so-called Fröhlich processes), as a means to realize a phonon bottleneck [6,8,9]. Among the main approaches being explored in this area, considerable effort has focused on developing materials with large atomic mismatch, as a means to induce a large phonon band gap and to thereby inhibit the dominant [10,11] energy-loss mechanisms for hot carriers in polar semiconductors. Elsewhere, low-dimensional systems, such as quantum wells [12] and dots [13], have been exploited, and have provided evidence for slowed carrier thermalization relative to their bulk counterparts. In this work, however, we are motivated by a very different approach, in which the storage and extraction of hot carriers has been proposed via the approach of *valley photovoltaics* (VPs) [7,14]. In this approach, the large built-in fields inside an appropriate solar cell are utilized to rapidly drive optically generated hot carriers from the main (conduction-band) valley of an appropriate semiconductor, into a satellite valley in which optical-phonon mediated energy loss is strongly suppressed.

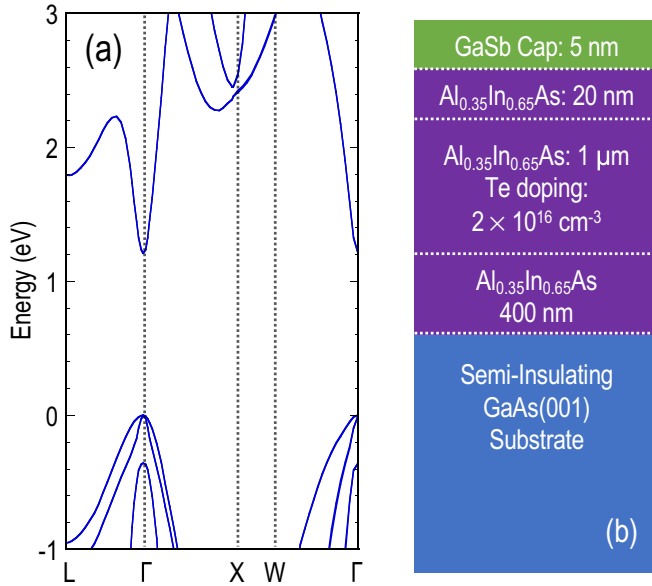


FIG. 1. (a) Band structure of  $\text{Al}_{0.35}\text{In}_{0.65}\text{As}$ , calculated at 300 K. The calculation is based upon the use of empirical pseudopotentials, adjusted to available experimental data on the optical properties of the material. See Refs. [7,19] for details. (b) Schematic layer structure (not to scale) of the  $\text{Al}_{0.35}\text{In}_{0.65}\text{As}$  films studied here.

By incorporating the absorbing layer into an appropriately designed multilayer cell [7], it should then be possible to extract the hot carriers from this more-energetic valley, allowing the long-sought potential of hot-carrier solar cells to be realized. Added to this, the use of relatively simple structures, based on bulk III-V absorbers, offers potential reductions in cost and complexity, relative to quantum-wire or quantum-dot systems.

It will be apparent from the discussion above that the choice of appropriate absorber material is critical to the realization of efficient VP cells. One material that has been attracting interest in this regard is the ternary  $\text{Al}_x\text{In}_{1-x}\text{As}$ , which has traditionally been used in a variety of optoelectronic applications, and as the barrier material in high-electron-mobility transistors [15–18]. Ferry has suggested that it is ideally suited to serve as the absorber of a VP device, allowing performance in excess of the Shockley-Queisser limit [7]. The rationale for utilizing this material derives from the form of its band structure, which we show in Fig. 1(a) [19]. From this figure we infer that (for  $x = 0.35$ , the level of alloying relevant here)  $\text{Al}_x\text{In}_{1-x}\text{As}$  is a direct semiconductor, with a corresponding band gap of  $\sim 1.2$  eV. Under thermal equilibrium, and close to room temperature, electrons in this material predominantly occupy the lowermost ( $\Gamma$ ) conduction valley. By subjecting them to high-field excitation, however, it should be possible to drive them into the nearby  $L$  valley, located some 0.8 eV above the  $\Gamma$  point. In a recent ensemble–Monte Carlo study of hot-electron dynamics in this material, Welland and Ferry [19] found that the lifetime for the relaxation of these carriers back to the  $\Gamma$  valley should be several picoseconds, considerably longer than the time required for them to exit a properly designed device [7]. Such results offer strong support for the viability of developing VPs based upon this material.

While the potential of  $\text{Al}_x\text{In}_{1-x}\text{As}$  as a candidate system for use in VPs has previously been noted [7,19], to the best of our knowledge there are few, if any, experimental reports of its high-field transport behavior. Such knowledge is clearly critical, however, to the proper design of photovoltaic cells based upon this material. Motivated by this need, in this work we undertake studies of high-field conduction in epitaxially grown  $\text{Al}_{0.35}\text{In}_{0.65}\text{As}$  films, over wide ranges of temperature (200–400 K) and applied electric field ( $E \leq 50$  kV/cm). Doping of this material with Te endows it with  $n$ -type character, allowing our high-field studies to directly explore the details of hot-electron intervalley transfer, relevant to the design of high-efficiency VP cells. By subjecting these films to rapid voltage pulses (as short as 50 ns), we demonstrate pronounced negative-differential conductance in their current-voltage (i.e., velocity-field,  $v_d - E$ ) characteristics. This behavior is reproduced by ensemble Monte Carlo calculations, which show good quantitative agreement with the results of the experiment and indicate that the negative-differential conductance arises from the transfer of hot carriers between the  $\Gamma$  and  $L$  valleys of the conduction band. Importantly, the transfer onsets for fields around 10 kV/cm, significantly lower than the built-in field expected under normal operating conditions in cells incorporating this material [14]. Our results therefore confirm the excellent potential of  $\text{Al}_x\text{In}_{1-x}\text{As}$  for use as the absorber material in hot-carrier solar cell technology.

## II. EXPERIMENTAL METHODS

### A. Sample preparation

$\text{Al}_{0.35}\text{In}_{0.65}\text{As}$  films, with the layer structure indicated in Fig. 1(b), were grown in a Veeco GENxplor molecular beam epitaxy system. [This particular alloying composition was chosen due to its favorable band structure for VPs [7,19], as supported by the calculations of Fig. 1(a)]. After the native oxide was thermally removed from a semi-insulating GaAs(001) substrate, under an As flux of  $7.7 \times 10^{-6}$  Torr, a 150-nm-thick GaAs homoepitaxial layer was grown at a substrate temperature of 550 °C (as measured by an infrared pyrometer). The growth then continued with the deposition of a 400-nm-thick  $\text{Al}_{0.35}\text{In}_{0.65}\text{As}$  layer at 470 °C, with an As/group-III element (Al and In) flux ratio of 8. Following this, a 1- $\mu\text{m}$ -thick Te-doped  $\text{Al}_{0.35}\text{In}_{0.65}\text{As}$  layer was grown with a nominal Te concentration of  $2 \times 10^{16} \text{ cm}^{-3}$ . After the growth of another thin (20-nm) undoped  $\text{Al}_{0.35}\text{In}_{0.65}\text{As}$  layer, the substrate temperature was reduced to 420 °C and a 5-nm-thick GaSb cap layer was deposited at an Sb flux of  $1.2 \times 10^{-6}$  Torr. Reflection high-energy electron diffraction was used to perform *in situ* monitoring during the epitaxial growth, as well as for deposition-rate calibration prior to the growth.

Samples were prepared for electrical measurement by defining appropriate mesa structures via photolithography and wet etching, with a phosphoric acid–based solution being used for the latter purpose. Ohmic contact to the doped layer of  $\text{Al}_{0.35}\text{In}_{0.65}\text{As}$  was achieved by depositing Ni/Ge/Au/Ni/Au (8-/24-/54-/14-/150-nm, respectively) metal multilayers on suitable contact pads (see Fig. 2), and performing rapid thermal annealing at 480 °C. Three different kinds of

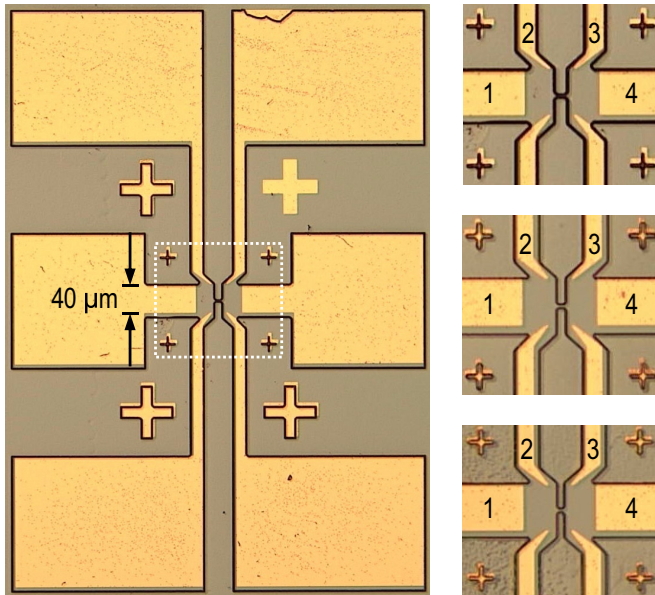


FIG. 2. Shown left is an optical micrograph of an etched constriction, configured to allow four-probe measurement of electrical behavior. Panels on the right are expanded views of the constriction area, formed in three different samples (the view is that enclosed by the white dotted line in the left panel). Upper panel: etched length =  $12.5 \mu\text{m}$ ; etched width =  $1.1 \mu\text{m}$ . Center panel: etched length =  $10.5 \mu\text{m}$ ; etched width =  $2.0 \mu\text{m}$ . Bottom panel: etched length =  $8.0 \mu\text{m}$ ; etched width =  $2.7 \mu\text{m}$ . In a four-probe measurement, external voltage is applied across the probes numbered 1 and 4 in each panel, while the resulting voltage drop across the constriction is measured between probes 2 and 3.

sample were processed for this study, with the first consisting of a simple Hall-bar geometry that was utilized for carrier concentration and mobility characterization. The second type of device is illustrated in Fig. 2, and was realized by using an appropriate photomask to define a narrow constriction at the center of a larger mesa. By defining a bottleneck for current flow, this geometry allows high electric fields ( $E > 10^4 \text{ V/cm}$ ) to be generated within the conducting layer, fields that may be probed using the contacts labeled 2 and 3 in the panels on the right of Fig. 2. The third type of sample was designed with an on-chip coplanar-waveguide geometry [20,21], to provide  $50\text{-}\Omega$  matching to the etched constriction. In this report, we present results from detailed studies of three different constrictions; the first two (referred to hereafter as 4P-1 and 4P-2) having etched length (width) of 10 and  $14 \mu\text{m}$  ( $0.2$  and  $8 \mu\text{m}$ ), respectively. The third device (denoted as CPW-1) utilized the coplanar geometry and had a constriction with an etched length (width) of  $10 \mu\text{m}$  ( $0.6 \mu\text{m}$ ). The orientation dependence of the transport, and its possible anisotropy, was not investigated here, but represents an interesting direction for future possible study.

### B. Electrical measurements

Dc and pulsed electrical characteristics were measured after mounting samples in a variable temperature cryostat, capable of covering the temperature range from 3 to 500 K. Dc measurements were made using a Keithley 2400 source

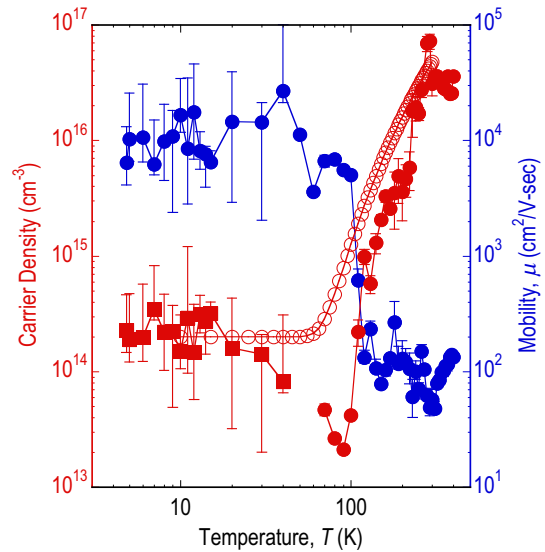


FIG. 3. Variation of carrier density (left axis, red symbols) and mobility (right axis, blue symbols), determined from Hall measurements of an  $\text{Al}_{0.35}\text{In}_{0.65}\text{As}$  Hall-bar sample. Empty (red) circles represent the results of calculations of the charge density (see main text for further details). Filled (red) squares denote hole density, filled (red) circles show electron density.

meter to apply a voltage  $V$  to the samples and measure the resulting current ( $I$ ). To determine the electron concentration and low-field mobility of the  $\text{Al}_{0.35}\text{In}_{0.65}\text{As}$  layers, we also performed Hall measurements via low-frequency ( $\sim 11 \text{ Hz}$ ) lock-in detection, with an ac excitation of  $\sim 100 \mu\text{V}$  and by placing the tail of our cryostat in the bore of a 0.4-T electromagnet.

Pulsed measurements were performed using a setup that we have described previously in a number of publications (see Refs. [20,21] for examples). In these measurements, the sample chips were mounted on FR-4 boards that enabled high-frequency (SMA) connections to be made, from chip level to the external electronics. A Berkeley Nucleonics Corp. Model 577A generator was then used to apply single-shot pulses with peak amplitude ( $V_p$ ) as large as 45 V to the samples, with the resulting transient variation of current being detected at the  $50\text{-}\Omega$  input of a mixed-signal oscilloscope (DSO-X 6000A Series; 6-GHz bandwidth; Keysight Technologies, Inc.). The high resistance of the constriction ( $> 10^5 \Omega$ ) meant that the applied voltage was dropped almost entirely across this structure.

## III. RESULTS AND ANALYSIS

### A. Carrier concentration and low-field mobility

In Fig. 3, we plot the temperature-dependent variation of the carrier (electron) concentration, and low-field mobility ( $\mu$ ), as determined for the Hall-bar sample over a wide range of temperature.

The Hall measurements show a crossover from hole to electron conduction as the temperature is varied, with the former dominating below  $\sim 100 \text{ K}$  where the donors freeze out. In this temperature range, the hole concentration

appears pinned around  $10^{14} \text{ cm}^{-3}$ , behavior that suggests the presence of an acceptor level in the material, close to the edge of the valence band. While the origin of these acceptors is currently unclear, defects (i.e., roughness) at the upper  $\text{Al}_{0.35}\text{In}_{0.65}\text{As}/\text{GaSb}$  interface are one possibility. Alternatively, compositional fluctuations in the  $\text{Al}_{0.35}\text{In}_{0.65}\text{As}$  alloy might also be responsible.

As the temperature is increased beyond 100 K, the donors become thermally activated and the carrier concentration rapidly increases to a level of a few  $10^{16} \text{ cm}^{-3}$  by 300 K, comparable to the doping density. With further increase of temperature to 400 K the carrier concentration then appears to saturate (or, possibly, even decrease slightly), confirming the notion that the material is in the extrinsic limit. Also shown in Fig. 3 is the calculated variation of the carrier density, assuming a background dopant concentration of  $2 \times 10^{14} \text{ cm}^{-3}$  (as indicated by the Hall measurements), and a Te dopant level of  $2 \times 10^{16} \text{ cm}^{-3}$ , with an ionization energy of approximately 60 meV. The standard form for compensated material [22,23] was used for this calculation, with no approximations. While the crossover from electron to hole conduction is not captured in this one-carrier model, the calculated variation of carrier concentration with temperature closely follows that in experiment at temperatures above 150 K.

In the discussion that follows, we will focus on an analysis of hot-carrier action in the range from 200 to 400 K. In this limit, since the transport is well described in terms of a single-carrier (i.e., electron) model we do not discuss further issues associated with the low-temperature ( $<100 \text{ K}$ ) regime of Fig. 3.

With regard to the variation of mobility presented in Fig. 3, in the region below 100 K, where the dopants are apparently unactivated, the mobility saturates at a level of around  $10\,000 \text{ cm}^2/\text{V s}$ . As the temperature is increased, and dopant activation is initiated, however, the mobility rapidly decreases, dropping to a level of around  $100 \text{ cm}^2/\text{V s}$  by 200 K, before then decreasing in a much slower manner. The coincidence of the sharp drop with the corresponding increase of carrier concentration is strongly suggestive of the role of ionized-dopant scattering.

### B. Dc characterization of etched constrictions

Dc characterization of etched films was performed as a means to confirm the influence of the constriction. In the main panel of Fig. 4, we compare the current-voltage characteristics of a film, before (blue data) and after (red data) the formation of a constriction (4P-2, of length  $14 \mu\text{m}$  and width  $8 \mu\text{m}$ ). The bulk film exhibits an almost linear variation of current, up to an applied voltage of 10 V. With the constriction formed, however, the current is reduced by a factor of around 20, and exhibits a more strongly nonlinear character, as evidenced in the lower inset. This plots the variation of current on an expanded scale and reveals a strongly nonlinear variation, with the first signs of current saturation being apparent by the time that the applied voltage reaches 2 V. The emergence of this nonlinearity is a consequence of the fact that the applied voltage is dropped primarily across the constriction, generating large electric fields ( $\sim 7 \text{ kV/cm}$  at 10 V) within it that lead to significant electron-phonon scattering.

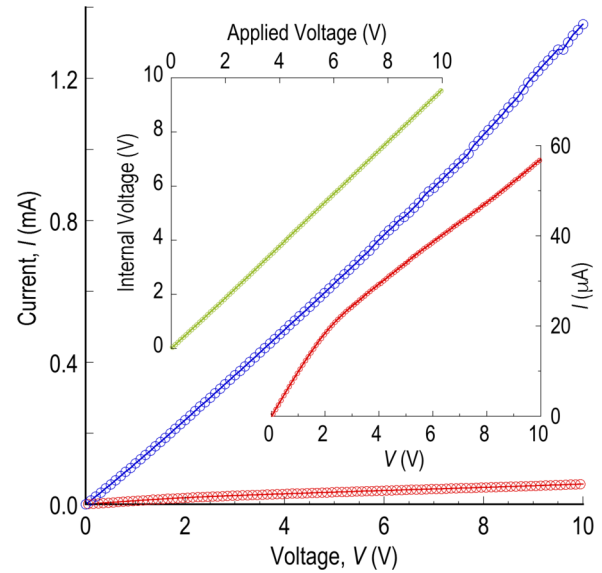


FIG. 4. The main panel plots the measured current-voltage characteristics of sample 4P-2, before (empty blue circles) and after (empty red circles) constriction etching. The lower inset is an expanded view of the data from the main panel, after the etching. The upper-left inset compares the voltage drop measured internally across the constriction (i.e., using probes 2 and 3 in Fig. 2), as a function of that applied to the sample (across probes 1 and 4). The slope of the resulting straight line is 0.960 with an  $R$  coefficient of 0.999 98.

An advantage of the multiprobe geometry shown in Fig. 2 is that it allows us to understand the manner in which the applied voltage is dropped in our structures, an important issue in high-field studies where loss of voltage at contacts can sometimes be problematic. In the upper inset of Fig. 4, we plot the voltage measured across the internal voltage probes, on either side of constriction 4P-2 (those labeled 2 and 3 in Fig. 2), as a function of the applied voltage. The resulting graph is a straight line with a slope extremely close to 1, over the entire range of the applied voltage. This outcome gives us confidence that the applied voltage in our experiments is dropped primarily across the formed constrictions.

Moving on to the quantitative form of the current-voltage characteristics obtained by dc biasing, in Fig. 5 we show the form of these measured for sample 4P-1, over a wide range of temperature (100–300 K). Regardless of the value of the applied voltage, the overall current level increases monotonically with temperature, an effect that arises predominantly from the corresponding increase in carrier concentration (see Fig. 3). Focusing on the behavior observed at fixed temperature, with increasing voltage a crossover from a linear variation to a saturation of the current is apparent, an evolution that is present at all temperatures but which is especially apparent at the 300-K end of the contour. The saturation is indicative of drift-velocity ( $v_d$ ) saturation, but reveals no evidence of the negative-differential conductance expected to result from intervalley ( $\Gamma$ - $L$ ) transfer. In order to observe this behavior, it is necessary instead to perform measurements via transient pulsing, as we now describe.

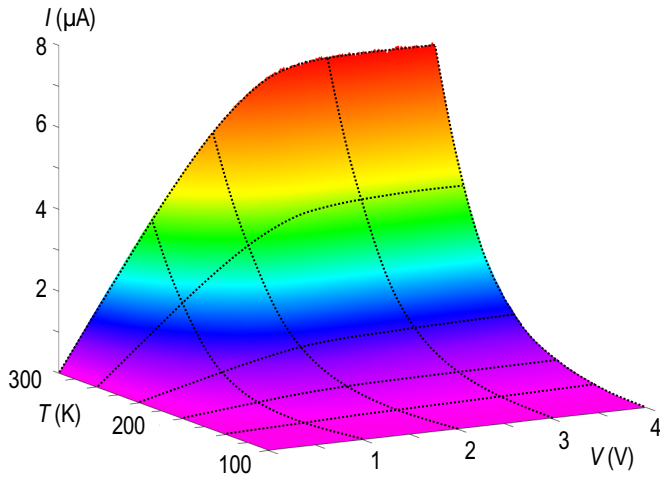


FIG. 5. Temperature-dependent current-voltage characteristics, determined for sample 4P-1.

### C. Transient pulsing of etched constrictions

In Fig. 6, we illustrate the influence of pulsing on the measured characteristics of sample 4P-1, comparing these with the behavior obtained by dc biasing. In Fig. 6(a), we illustrate the form of the transient voltage recorded for applied pulses of varying duration, ranging from 50 ns to 500  $\mu$ s. The waveforms all show significant transients at their rising and falling edges, features that are parasitic signals associated with the large resistance ( $\sim 10^5 \Omega$ ) of the constriction. The presence of these transients limited the shortest pulse duration that could reliably be utilized in the experiments to 50 ns; as we indicate in Fig. 6(a), for this timescale, the pulse was long enough to ensure that the initial overshoot at its rising edge became fully damped, prior to determining a steady voltage by the end of the pulse. As the pulse duration is increased from 50 ns to 500  $\mu$ s in Fig. 6(a), it is clear that the final output voltage (proportional to the current) decreases. This effect of heating gives rise to a pronounced dependence of the current-voltage characteristic on pulse duration, as we demonstrate in Fig. 6(b). This shows how pulsing yields a significant increase in current level over dc biasing, an effect that becomes more prominent as the pulse duration is reduced. (This is found to be a general feature of our experiments; see the results of Fig. 7, for example.) At the same time, the shorter pulsed characteristics reveal a clear region of negative-differential conductance, which onsets around 8 – 10 V and which also becomes more pronounced as the pulse length is shortened (from 0.5 ms to 50 ns). The negative-differential conductance is suggestive of ( $\Gamma$ -L) intervalley scattering [7,19], and its emergence as pulse duration is reduced can presumably be attributed to a corresponding reduction of Joule heating in the constriction. Indeed, the observation that longer pulses yield only current saturation, while shorter ones resolve the negative-differential conductance, is common in studies of high-field intervalley scattering. In experiments on the Gunn effect, for example, electric-field domains form when longer pulses are applied, masking the negative-going regions of the conductance [24].

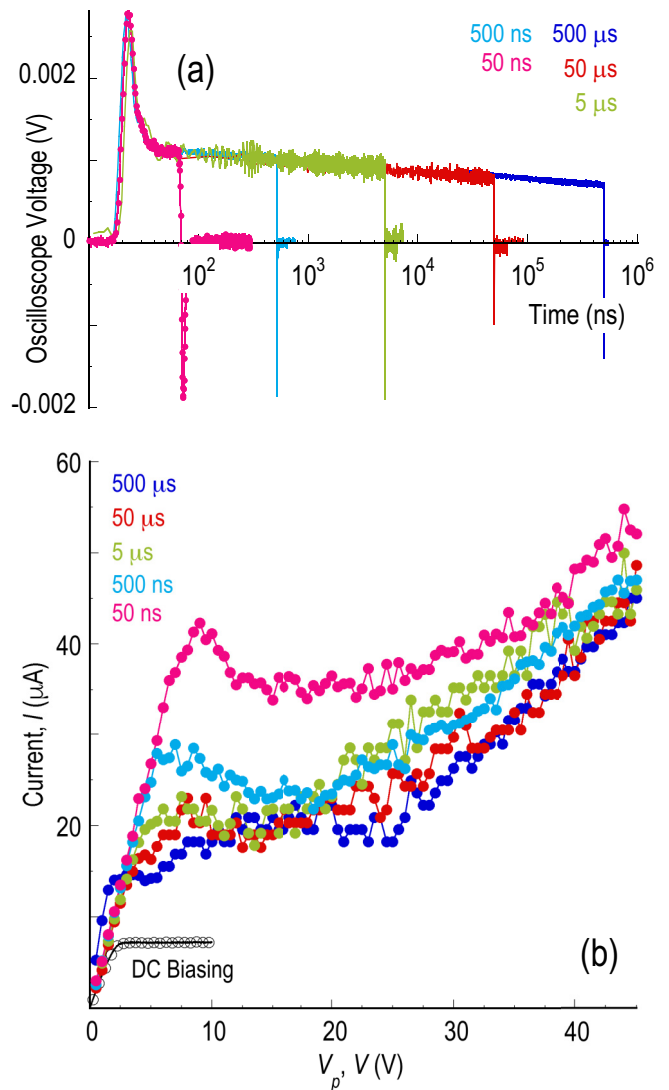


FIG. 6. (a) Single-shot pulses of varying duration, measured at the 50- $\Omega$  input of the oscilloscope. The measurements were performed on sample 4P-1 at room temperature, and the input-pulse amplitude was 4.0 V in each measurement. (b) Comparison of transient pulsing and dc biasing. The solid symbols were obtained from single-shot pulses such as those of panel (a). The value of the current plotted in panel (b) is that recorded at the end of the corresponding pulse, after any parasitic-related transients had died down.

In Fig. 7, we summarize the results of a detailed, temperature-dependent study of the negative-differential conductance in CPW-1. In these measurements, the pulse duration was held fixed at 50 ns (the shortest time for which we could obtain reliable measurements of the high-impedance constriction), while the amplitude was incremented up to as much as 45 V. In the lower part of the figure, we show three line plots that correspond to the results of measurements at the representative temperatures of 250, 300, and 350 K, from left to right, respectively. While these each exhibit similar qualitative characteristics, it will be noted that the overall current level increases with increasing temperature, similar to

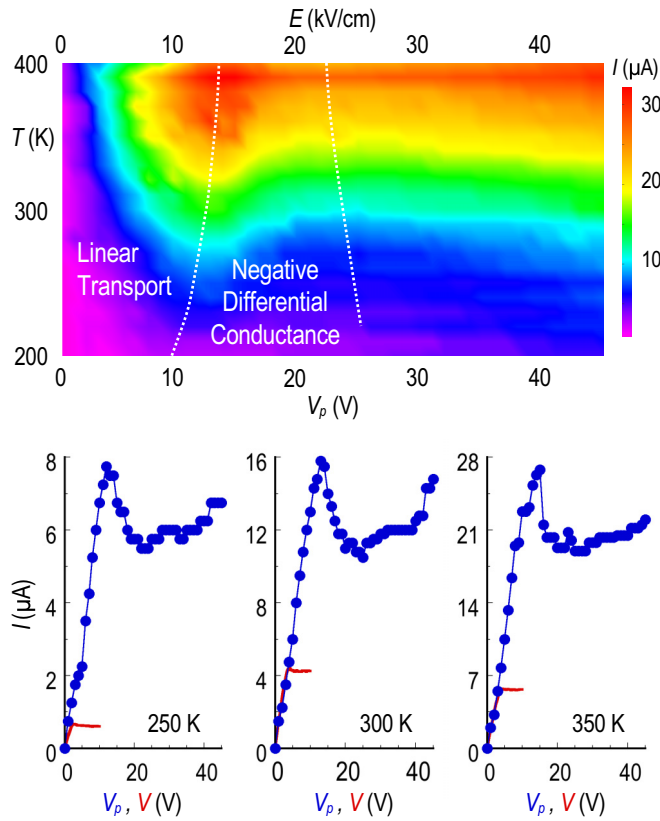


FIG. 7. Negative-differential conductance in sample CPW-1. The upper panel is a color contour showing the variation of current as a function of temperature and pulsed voltage (or corresponding electric field; see upper axis). The range of the regions of linear transport and negative-differential conductance are approximately denoted by white dotted lines. Pulse duration was 50 ns in all cases. The line plots at the bottom compare the pulsed current (blue filled symbols) with that obtained from dc biasing (red line), at three representative temperatures (250, 300, and 350 K, from left to right, respectively).

the behavior seen earlier in Fig. 5. In all three panels, we again see that the pulsed current rises to a significantly higher value than its dc counterpart, the latter of which typically saturates for an applied voltage ( $V$ ) below 5 V. As indicated by the white dotted lines in the contour of Fig. 7, the range of negative-differential conductance widens at lower temperatures. This behavior is quite common to systems exhibiting negative-differential conductance [23,24], in which, as temperature is reduced, two effects combine to enhance the visibility of the negative-differential excursion. The first is an increase of the low-field mobility (as in Fig. 3), which reduces scattering within the initial valley and thereby enhances the influence of the intervalley processes. At the same time, and as with other scattering, the reduction of the Bose-Einstein factor causes the intervalley scattering to weaken as the temperature is lowered, and this also contributes to the widening of the range for negative-differential conductance.

#### D. Modeling hot-carrier transport in $\text{Al}_{0.35}\text{In}_{0.65}\text{As}$

For insight into the physical origins of the behavior revealed in our experiments, calculations of high-electric-field

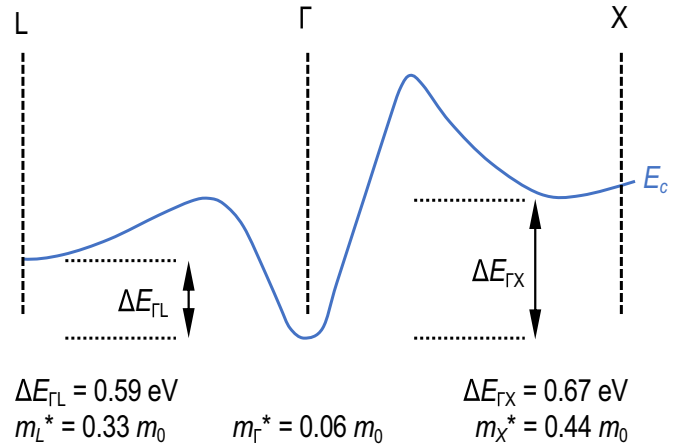


FIG. 8. Schematic illustration of the conduction-band structure of  $\text{Al}_{0.35}\text{In}_{0.65}\text{As}$  utilized in our Monte Carlo calculations. The local minimum in the conduction band that defines  $\Delta E_{\Gamma X}$  is located some 85% of the way to X, along the (100) direction. For further details, we refer the reader to Ref. [19].

transport were performed by the ensemble Monte Carlo method, using a three-valley band structure with nonparabolic character [19] (see schematic of Fig. 8).  $\text{Al}_{0.35}\text{In}_{0.65}\text{As}$  is a direct-gap semiconductor in which electrons predominantly occupy the  $\Gamma$  valley [see Fig. 1(a)] under thermal equilibrium at room temperature. When a sufficient electric field is applied, however, electrons may scatter into the side ( $L$  and  $X$ ; see Fig. 8) valleys, and it is this behavior that is responsible for the negative-differential conductance [14]. To describe this behavior, scattering from impurities, from the polar-optical and acoustic phonons, and from the random atomic potential resulting from alloying, were all included in the calculations. For the polar modes, an effective average of the dielectric properties of InAs and AlAs was used [23,25] to give a single effective polar interaction. The scattering also included the appropriate intervalley processes, between the  $\Gamma$  and  $L$  valleys, the  $L$  and  $X$  valleys, and the  $X$  and  $\Gamma$  valleys, as well as among each set of equivalent valleys. The intervalley rates are more than an order of magnitude larger than the polar scattering [19], so that with sufficient energy they are far more likely to be scattered to the  $L$  valleys than to relax by polar phonon emission.

Monte Carlo calculations were performed at a series of electric fields, in each case for sufficient time to allow the distribution function to settle into its steady state, but under the assumption that the electric field remains constant throughout this period. While the inhomogeneous electric field that can arise from domain formation is easily simulated in complete device simulations, this was not done here, where our main interest was in the negative-differential conductance and its connection to the different valley populations. Typical simulation times were a few tens of picoseconds, incorporating some  $10^5$  particles and with ensemble averages typically performed every 0.1 ps. The drift velocity ( $v_d$ ), valley densities, and distributions were then determined at each value of the electric field ( $E$ ), and for each time step of the ensemble averages.

In Fig. 9(a), we compare the calculated (room-temperature) velocity-field curve of  $\text{Al}_{0.35}\text{In}_{0.65}\text{As}$  with the results of our

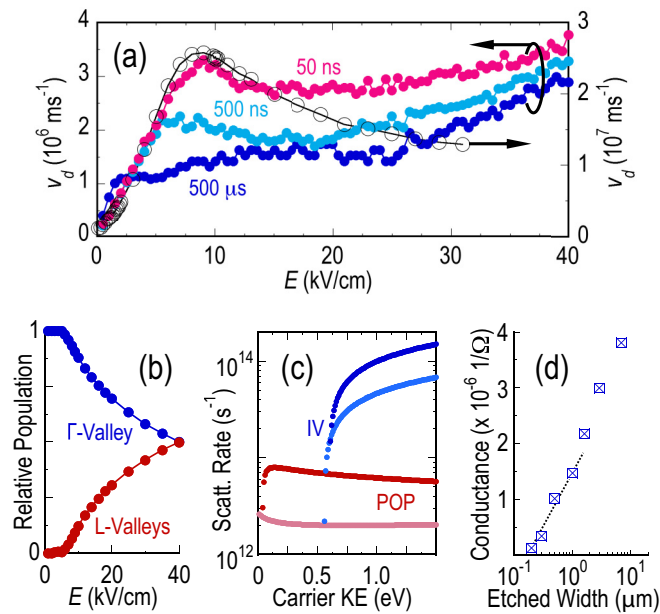


FIG. 9. (a) Comparison of experimental velocity-field ( $v_d - E$ ) curves (filled symbols, left axis) with the results of ensemble Monte Carlo simulations (open symbols, right axis). Experimental data were obtained from the results of Fig. 6, while the Monte Carlo calculations were performed at 300 K. Note the different scales on the left and right axes. (b) Calculated relative populations of the  $\Gamma$  and  $L$  valleys at 300 K, as a function of electric field. (c) Calculated scattering rates for polar optical phonons (POP) and for intervalley transfer (IV). The lower (upper) curve for each mechanism describes phonon absorption (emission). (d) Variation of measured low-field conductance for etched constrictions of varying physical width. The dotted line extrapolates to an etched width of  $\sim 175$  nm for zero conductance.

experiments. In the latter case, the data shown were calculated from the pulsed characteristics of Fig. 6, and from a knowledge of the constriction geometry and the carrier concentration (Fig. 3) at room temperature. As the pulse duration is shortened, and Joule heating is suppressed, the experimental data clearly develop a form that increasingly approximates the results of our calculations. In addition, the longer pulses are more susceptible to the generation of a high-field domain, which may pin at the anode and mask the negative conductance in the curves [24]. Most notable is the emergence of the negative-differential current (or velocity), which onsets around 10 kV/cm in agreement with our calculations. In Fig. 9(b), we illustrate the connection of the negative-differential conductance to intervalley transfer, by plotting the relative populations of the  $\Gamma$  and  $L$  valleys as a function of electric field. At thermal equilibrium ( $E = 0$ ), we see that electrons predominantly reside in the lower ( $\Gamma$ ) conduction-band valley, and that their transfer to the  $L$  valleys is initiated for fields as low as 5 kV/cm. The onset of negative-differential velocity, above 10 kV/cm in Fig. 9(a), is then clearly correlated to a growth of the population in the  $L$  valleys. (The population of the  $X$  valleys, which lie 80 meV above the  $L$  valleys, remains quite low over this range of fields and is therefore not indicated in this figure [14].)

A crucial feature of the intervalley (IV) transfer described above is that, once it onsets, it dominates over energy loss via polar optical phonon (POP) scattering, allowing the proposed “storage” of energetic carriers in the side valleys. This point is emphasized in Fig. 9(c), where we show the energy dependence of the IV and POP scattering mechanisms. This figure shows that IV scattering grows dramatically as the carrier energy is increased beyond  $\sim 0.6$  eV, a value that compares well with the  $\Gamma$ - $L$  valley separation in the band structure [see Fig. 1(a)]. With further increase of carrier energy, the IV scattering rate grows to a value almost 30 times larger than that of POP scattering, allowing the former mechanism to dominate. The crucial implication for hot-carrier solar cell action is that, as the carriers scatter into the  $L$  valley, their kinetic energy is converted largely to potential energy, preventing subsequent energy loss via significant optical-phonon emission. This should be contrasted with the situation where the energetic electrons remain in the  $\Gamma$  valley, in which case thermalization after acceleration to a kinetic energy of 0.6 eV would result in the cascading emission of some 30 optical phonons.

One aspect of Fig. 9(a) that becomes clear upon closer inspection is that the experimentally determined drift velocities (and low-field mobilities) are systematically lower than the calculated ones, by approximately an order of magnitude (note the different scales on the left and right axes). There are a number of factors that might be responsible for this, beginning with uncertainty in the precise constriction geometry. Specifically, the influence of surface depletion at the etched boundaries of the constrictions is not considered in our calculation of the experimental current density, and should therefore lead to a systematic underestimation of the current density (and so of the velocity). To account for this depletion, in Fig. 9(d) we plot the variation of the low-field conductance as a function of the etched width of a number of different constrictions. The various data points plotted here were measured in a probe station, under ambient conditions, and were calculated from the linear portion of the current-voltage characteristic around zero bias. The data show (see the dotted line) that the conductance extrapolates to zero for an etched width of  $\sim 175$  nm, a value that should correspond to the full extent of the edge depletion in these structures. Accounting for this depletion in the data of Fig. 9(a), the current density increases by a factor of around 4, yielding a similar increase in the drift velocity. For the 50-ns pulses, for example, the peak velocity (at  $\sim 9$  kV/cm) increases from  $3.5 \times 10^6$  cm/s to  $1.3 \times 10^7$  cm/s, reaching a value that is around 50% of that predicted theoretically [see Fig. 9(a)].

Another factor contributing to the difference between the measured and predicted drift velocities is due to heating. This is clearly seen in Fig. 9(a), where the peak velocity increases with reduced pulse duration. In our experiment, as we have noted already, the high constriction resistance ( $> 10^5 \Omega$ ) prevented us from performing measurements using shorter pulses. Nonetheless, the indication from Fig. 9(a) is that such measurements could be expected to yield further increases in the peak velocity, possibly ultimately approaching the computed value. (Indeed, even the 50-ns pulse is not immune from the formation of the electric field domain at the anode. This would result in a lower observed peak velocity as

well as the rising current at higher fields, where it is apparent from Fig. 9(a) that the current deviates significantly from the continuing decrease of the velocity at the highest fields.)

#### IV. CONCLUSIONS

In conclusion, the multivalley conduction-band structure of  $\text{Al}_{0.35}\text{In}_{0.65}\text{As}$  has been proposed for use in so-called *valley photovoltaics*, in which energetic photocarriers are stored in satellite valleys, allowing them to be extracted prior to thermalization. To explore this application, in this work we have undertaken a detailed characterization of the electrical properties of Te-doped (*n*-type)  $\text{Al}_{0.35}\text{In}_{0.65}\text{As}$ , over wide ranges of temperature (3–400 K) and electric field (<50 kV/cm). Using pulsed measurements to suppress the influence of Joule heating, we revealed the presence of clear negative-differential conductance in the current-voltage characteristics of the films, suggestive of the intervalley transfer of hot electrons. This conclusion was supported by the results of ensemble Monte Carlo simulations of the hot-carrier action,

which established the connection of the negative-differential conductance to hot-electron transfer between the  $\Gamma$  and *L* valleys. The quantitative features of the experimentally determined velocity-field curves were found to be in good agreement with these calculations, providing further confidence in the role of the implied intervalley transfer mechanism. Importantly, the transfer onsets for fields around 10 kV/cm, significantly lower than the expected built-in fields ( $\sim 35$  kV/cm) in cells incorporating this material [7]. Overall, these results confirm the excellent potential of  $\text{Al}_{0.35}\text{In}_{0.65}\text{As}$  for use as the absorber material in hot-carrier solar cell technology.

#### ACKNOWLEDGMENTS

Work at Buffalo was supported by U.S. Department of Energy, Office of Basic Energy Sciences, Division of Materials Sciences and Engineering under Award No. DE-FG02-04ER46180. The  $\text{Al}_{0.35}\text{In}_{0.65}\text{As}$  films were grown at the University of Oklahoma using a GENxplor MBE system acquired with support from the NSF through Grant No. DMR-1229678.

- 
- [1] M. A. Green, *Prog. Photovoltaics* **9**, 123 (2001).
- [2] B. Ehrler, M. W. B. Wilson, A. Rao, R. H. Friend, and N. C. Greenham, *Nano Lett.* **12**, 1053 (2012).
- [3] O. E. Semonin, J. M. Luther, S. Choi, H.-Y. Chen, J. Gao, A. J. Nozik, and M. C. Beard, *Science* **334**, 1530 (2011).
- [4] Y. Okada, N. J. Ekins-Daukes, T. Kita, R. Tamaki, M. Yoshida, A. Pusch, O. Hess, C. C. Phillips, D. J. Farrell, K. Yoshida, N. Ahsan, Y. Shoji, T. Sogabe, and J. F. Guillemoles, *Appl. Phys. Rev.* **2**, 021302 (2015).
- [5] W. Shockley and H. J. Queisser, *J. Appl. Phys.* **32**, 510 (1961).
- [6] R. T. Ross and A. J. Nozik, *J. Appl. Phys.* **53**, 3813 (1982).
- [7] D. K. Ferry, *Semicond. Sci. Technol.* **34**, 044001 (2019).
- [8] J. A. R. Dimmock, M. Kauer, K. Smith, H. Liu, P. N. Stavrinou, and N. J. Ekins-Daukes, *J. Opt.* **18**, 074003 (2016).
- [9] G. Conibeer, N. Ekins-Daukes, J.-F. Guillemoles, D. Konig, E.-C. Cho, C.-W. Jiang, S. Shrestha, and M. Green, *Sol. Energy Mater. Sol. Cells* **93**, 713 (2009).
- [10] P. Klemens, *Phys. Rev.* **148**, 845 (1966).
- [11] B. K. Ridley, *J. Phys.: Condens. Matter* **8**, L511 (1996).
- [12] Y. Rosenwaks, M. C. Hanna, D. H. Levi, D. M. Szymd, R. K. Ahrenkiel, and A. J. Nozik, *Phys. Rev. B* **48**, 14675 (1993).
- [13] Y. Harada, N. Iwata, S. Ashai, and T. Kita, *Semicond. Sci. Technol.* **34**, 094003 (2019).
- [14] H. Esmailpour, K. R. Dorman, D. K. Ferry, T. D. Mishima, M. B. Santos, V. R. Whiteside, and I. R. Sellers, *Nat. Energy* **5**, 336 (2020).
- [15] M. P. Lumb, M. Gonzalez, M. K. Yakes, C. A. Affouda, C. G. Bailey, and R. J. Walters, *Prog. Photovoltaics* **23**, 773 (2015).
- [16] M. S. Leite, R. L. Woo, J. N. Munday, W. D. Hong, S. Mesropian, D. C. Law, and H. A. Atwater, *Appl. Phys. Lett.* **102**, 033901 (2013).
- [17] B. L. Smith, Z. S. Bittner, S. D. Helistroem, G. T. Nelson, M. A. Slocum, A. G. Norman, D. V. Forbes, and S. M. Hubbard, *Prog. Photovoltaics* **25**, 706 (2017).
- [18] P. Li, H. Tang, T. Li, X. Li, X. Shao, T. Pavelka, L. Huang, and H. Gong, *J. Electron. Mater.* **46**, 2061 (2017).
- [19] I. Welland and D. K. Ferry, *Semicond. Sci. Technol.* **34**, 064003 (2019).
- [20] H. Ramamoorthy, R. Somphonsane, J. Radice, G. He, C.-P. Kwan, and J. P. Bird, *Nano Lett.* **16**, 399 (2016).
- [21] J. Nathawat, K. K. H. Smithe, C. D. English, S. Yin, R. Dixit, M. Randle, N. Arabchigavkani, B. Barut, K. He, E. Pop, and J. P. Bird, *Phys. Rev. Mater.* **4**, 014002 (2020).
- [22] J. S. Blakemore, *Semiconductor Statistics* (Pergamon Press, Oxford, 1962), Sec. 3.3.
- [23] D. K. Ferry, *Semiconductors: Bonds and Bands*, 2nd ed. (IOP Publishing, Bristol, 2020).
- [24] M. P. Shaw, H. L. Grubin, and P. R. Solomon, *The Gunn-Hilsum Effect* (Academic Press, New York, 1979).
- [25] A. G. Milekhin, A. K. Kalagin, A. P. Vasilenko, A. I. Toropov, N. V. Surovtsev, and D. R. T. Zahn, *J. Appl. Phys.* **104**, 073516 (2008).